Seasonal Modulations and Propagation of Subantarctic Mode Water Potential Vorticity[*]

Sunke Schmidtko[1] and Gregory C. Johnson
National Oceanic and Atmospheric Administration, Pacific Marine
Environmental Laboratory, Seattle, Washington

for *Journal of Physical Oceanography*

[1] *Corresponding author address*: Sunke Schmidtko, *National Oceanic and Atmospheric Administration, Pacific Marine Environmental Laboratory, 7600 Sand Point Way NE, Seattle, Washington 98115 Email: sunke.schmidtko@noaa.gov*

Abstract

Subantarctic Mode Water (SAMW) is formed in late austral winter along the northernmost front of the Antarctic Circumpolar Current (ACC), most prominently in the Indian and Pacific oceans. One distinctive feature of the SAMW is its annually renewed pycnostad, a pronounced minimum in the absolute value of potential vorticity ($|\Pi|$) that distinguishes the SAMW from surrounding water masses. After subduction SAMW spreads northward, ventilating mid-depth subtropical and tropical waters at the base of the permanent pycnocline. Here the seasonal evolution of SAMW $|\Pi|$ structure is analyzed using data from the Argo array of freely drifting, profiling CTD floats. The core potential density anomaly of the SAMW pycnostad increases from west to east, from $\sigma_\theta = 26.68$ kg m^{-3} in the western Indian Ocean to 27.0 kg m^{-3} around Drake Passage. Seasonal $|\Pi|$ anomalies of amplitude ~4 × 10^{-12} m^{-1} s^{-1} within the SAMW propagate at phase speeds of 2.5 to 10 cm s^{-1} on five core isopycnals spanning SAMW in the Indian and Pacific oceans. These phase speeds apparently exceed current velocities estimated on these isopycnals by combining direct velocities from Argo float displacement data with geostrophic estimates from Argo density data. Phase speeds are lowest at midlatitudes and increase towards the equator when roughly following streamlines of the velocity field. These $|\Pi|$ anomalies near the base of the permanent pycnocline could be thought of as 2nd baroclinic mode structures, and exhibit phase propagation similar to predictions for these modes.

1.   Introduction

Subantarctic Mode Water (SAMW; McCartney 1977) is a thick layer of water with relatively vertically homogenous properties (hence a mode) found equatorward of the northernmost front of the Antarctic Circumpolar Current (ACC), the Subantarctic Front (SAF), in the Southern Hemisphere. Varieties of SAMW are subducted at the southern edges of the subtropical gyres, and move generally northward and westward, ventilating the bases of the Southern Hemisphere subtropical thermoclines (Hanawa and Talley 2001). The formation and subduction of SAMW arises from a complicated interplay among winter-atmospheric buoyancy loss, northward Ekman transport, lateral induction, mixing, and eddy processes (Rintoul and England 2001, Karstensen and Quadfasel 2002, Salle et al. 2006, 2010, Koch-Larrouy 2010, Sloyan et al. 2010; Herraiz-Borreguero and Rintoul 2011).

Perhaps the most prominent structure found in all varieties of SAMW is a pycnostad (Seitz 1967), a thick layer of relatively vertically uniform density (McCartney 1977). This structure is strongest just north of the SAF, diminishing to the north, but distinct to about 20°S in places, north of which it is completely eroded. This pycnostad corresponds by definition to a local vertical extremum in planetary potential vorticity, Π $= f/\rho\ (\partial\rho/\partial z)$, where f is the Coriolis parameter, ρ is potential density referenced to the central depth over which its vertical gradient is estimated, and z is depth. This quantity has the advantage of being conserved in inviscid geostrophic flows (Pedlosky 1987). While Π is negative in the Southern Hemisphere, we take its absolute value throughout

for convenience. Henceforth when we refer to the vertical minimum of this quantity in the SAMW, we have its absolute value in mind.

As mentioned above, a complex interaction of processes lead to SAMW formation and subduction. Nonetheless, subduction itself is fundamentally tied to the seasonal cycle, imparting a strong signature of the densest (and thickest) late-winter mixed-layer properties to the water mass being subducted (Stommel 1979). After subduction, conservative water mass properties including Π would be preserved in an inviscid flow (Pedlosky 1987), but are in reality modified by mixing processes. For all varieties of SAMW the low core values of $|\Pi|$, being local vertical and lateral extrema, will erode (increase in magnitude) with distance in space and time from their subduction site. Furthermore, one might expect some seasonal modulation of SAMW properties as the large-scale circulation of the subtropical gyres continues year-round while SAMW subduction is predominantly a late-winter phenomenon.

Here we study seasonal modulations of $|\Pi|$ within the SAMW of the Indian and Pacific oceans using hydrographic and velocity data from the Argo array of profiling CTD floats (Roemmich et al. 2009). In the Atlantic the data distribution, a complex circulation, and the generally sparse low $|\Pi|$ waters around the Atlantic SAMW confound the analysis. After a brief discussion of the mean structure of the SAMW, we focus on the spreading and propagation of these anomalies in $|\Pi|$ downstream from the regions where SAMW is subducted. We attempt to relate these anomalies to the mean geostrophic flow field, finding that the anomaly phase speeds somewhat exceed the large-scale circulation velocities.

2.   Data and methods

We use all available quality-controlled Argo float data downloaded from an Argo Global

Data Assembly Center in March 2010. We restrict our analysis to data flagged as good

(quality flag 1). Delayed-mode data are used as available, otherwise real-time data are

used. For individual float profiles potential temperature (θ), salinity (S) and pressure (P)

are interpolated onto potential density anomaly (σ_θ) levels at 0.02 kg m^{-3} intervals.

During this process, salinity and pressure data that lie outside 3 times the interquartile

range relative to the first and third quartiles within local bins are rejected as extreme

outliers.

On each isopycnal level we map these quantities (regardless of year) onto a 1

month x 1° latitude x 1° longitude climatological grid using a LOESS filter, a weighted

local 2nd order polynomial regression (Cleveland and Devlin 1988). The temporal cut-off

radius of the filter is three months and the horizontal radii are adaptive. The zonal radius

is twice that of the meridional radius owing to the strong zonal nature of features in the

interior of the Southern Ocean, although this choice slightly distorts the mapped fields

near eastern and western boundaries. The mapping uses the closest 2800 data points,

with a lower threshold for the meridional cut-off radius of 3.5° latitude, expanding to an

upper threshold of 7.5° as necessary to reach (or in very data-sparse regions, approach)

the 2800 data point target. Grid points in the climatology that have a sum of all weights

<100 or a LOESS-weighted distance from the grid point more than 0.8 times the

maximum cut-off radius are removed.

We calculate $|\Pi|$ for each grid point at 0.02 kg m^{-3} intervals (between each pair of

σ_θ levels). Geostrophic velocity calculations are done on a 2-dbar pressure grid using a

depth-interpolated version of the isopycnal climatology. These velocities are initially referenced to a 1000-db zero-velocity surface. We make the referenced geostrophic velocities absolute using a velocity field constructed from the 1000-dbar float displacements in the YoMaHa raw data set (Lebedev et al. 2007), downloaded in March 2010. The resulting velocities are then linearly interpolated onto the center of each $|\Pi|$ isopycnal range. We apply the same mapping scales and technique to these displacement data as for the isopycnal float climatology, but generating a single mean (data mapped regardless of date). Hence we assume little seasonal flow variability at 1000 dbar, as holds in the ocean interior south of 15ºS (Davis 2005).

Isopycnal climatologies like that which we analyze here better represent water-properties than isobaric ones, especially near strong fronts like the Gulf Stream or the ACC (Lozier et al. 1994). This improved representation is crucial for the SAMW, with its strong meridional isopycnal slopes and water-property gradients. We make no attempt to join the subsurface (ocean interior) isopycnal climatology we construct here to a mixed layer, so the upper bound of our climatology lies just below the seasonal mixed layer density (mapped from near-surface data, again using a LOESS filter). This neglect is acceptable as we are focusing only on processes and properties of SAMW following subduction along isopycnals.

3. SAMW structure

Properties at the core of the SAMW vary significantly spatially (Fig. 1). We define the core of SAMW as the vertical minimum in $|\Pi|$ below the seasonal pycnocline and shallower than 800 m (to exclude weakly stratified deep waters well outside the realm of the SAMW). We limit our analysis of SAMW thickness and volume to regions with $|\Pi|$

$< 50 \times 10^{-12}$ m^{-1} s^{-1}, a fairly stringent limit. The local thickness of SAMW is estimated as the depth difference of the lightest and densest isopycnal that fit the above criteria at each location.

The values of σ_θ at the SAMW core (Fig. 1a, black lines) near the ACC are lightest in the southwestern Indian Ocean (26.65 kg m^{-3}) and trend progressively denser towards the east, with small remnants of a density of 27.1 kg m^{-3} in the eastern Pacific near Drake Passage. Due to sparse data and complex South Atlantic Ocean structure we do not analyze the densest value (27.2 kg m^{-3}) that fits our $|\Pi|$ and depth criteria in the southwestern Atlantic Ocean. Core values of θ (Fig. 1a, white lines) drop monotonically from 12°C to 4°C and of S (Fig. 1b, white lines) from 35.2 to 34.2 PSS-78 over the same geographical range, hence the cooling counteracts and dominates the freshening to increase the density at the SAMW core progressing eastward from the southwestern Indian Ocean (e.g. McCartney 1977).

Values of the $|\Pi|$ minimum (Fig. 1b, colors) at the SAMW core also vary spatially. The lowest values are generally found just north of the ACC, and magnitudes increase to the north. However, there are east-west variations as well. The lowest values are found south of Australia and in the central and eastern South Pacific Ocean, areas previously identified as specific SAMW formation regions (e.g. Salle et al. 2010). The values in the Atlantic are relatively high; the SAMW signal there is less clear. The very deep dense values shown may not be SAMW. No values fall below our upper $|\Pi|$ limit in the western parts of the Indian and Pacific oceans, where the Agulhas and East Australia western boundary currents of the subtropical gyres introduce more stratified subtropical waters from the north. The region with the thickest $|\Pi| < 50 \times 10^{-12}$ s^{-1} m^{-1} layer (Fig. 1a,

colors) is the Southwest Pacific, between the regions of lowest core $|\Pi|$, suggesting that the location with the most SAMW is not necessarily a primary formation region, but may be a region of SAMW accumulation.

The depth of the core $|\Pi|$ values (Fig. 1b, black lines) generally deepens to the north, at least partly a reflection of the large-scale circulation, which influences isopycnal depths. Erosion of the core from above by more stratified subtropical waters to the north could also contribute to this pattern. This hypothesis is supported by the increase of the density of the core $|\Pi|$ values (Fig. 1a, black lines), and the increase of the magnitude of the core $|\Pi|$ values (Fig. 1b, colors), to the north.

A quasi-zonal vertical section of $|\Pi|$ (Fig. 1c, colors) with σ_θ (Fig. 1c, black lines) constructed following the meridional minimum in core SAMW $|\Pi|$ values just north of the SAF and within the subduction regions (Fig. 1c, red line near top with gray continents for orientation) allows another perspective on the varieties and zonal evolution of SAMW just discussed. Distinct pools of SAMW of differing properties south of Australia, the Tasman Sea, the central South Pacific, and the eastern South Pacific are apparent (Herraiz-Borreguero and Rintoul 2011). The radically different nature of the densest $|\Pi|$ minimum in the South Atlantic is also clear.

4.   Seasonal modulation of the $|\Pi|$ minimum

As mentioned above, one might expect some seasonal modulation of SAMW properties given that SAMW subduction is an annually recurring, predominantly late-winter phenomenon. Imagine a recurring seasonal cycle with no interannual variability and a steady gyre circulation. One would expect a seasonal modulation of the $|\Pi|$ minimum at

the core of SAMW near its formation region, with lower absolute values in late winter. This modulation, in combination with steady advection away from the formation region by the general circulation, would result in a propagation of low $|\Pi|$ anomalies downstream of the region, appearing schematically like proverbial $|\Pi|$ anomaly pigs in a SAMW python (Fig. 2). At any given point downstream these passing anomalies would be manifested locally as an annual modulation of $|\Pi|$ within the SAMW. This scenario is here investigated in relatively thin density layers within the SAMW, rather than for the entire thickness of the SAMW.

We fit an annual harmonic to the monthly climatological $|\Pi|$ values at each location to better determine the month in which the $|\Pi|$ value reaches its smallest magnitude there. This approach guards against classifying a $|\Pi|$ spike towards small magnitude in a single month arising from noise as the month of the minimum. However, selecting the month with the minimum magnitude instead of using the harmonic analysis does not significantly alter the resulting maps of $|\Pi|$ minimum phase visually. Depending on the isopycnal, 30-40% of the climatology grid points have monthly values that correlate with the annual harmonic above 0.8, with fewer grid points in each successive correlation bin below 0.8 (Fig. 3). All isopycnals have fewer than 25% of grid points with a correlation of 0.5 or less.

The locations of the local $|\Pi|$ minimum within the SAMW around early September (Fig. 4, left panels, black patches) show fairly distinct banded patterns oriented roughly perpendicular to the geostrophic flow (Fig. 4, left panels, green arrows) on five different isopycnals: two in the Indian and three in the Pacific Ocean. Magnitudes

of $|\Pi|$ (Fig. 4, left panels, blue contours) are generally lowest to the south near the

SAMW origins and increase with distance from the source.

The aggregate of local de-meaned annual variations of $|\Pi|$ aligned by the months

of their maximum values (Fig. 4, right panels) illustrates again the robust annual cycle of

$|\Pi|$ within the SAMW (see also Fig. 3). However, the amplitude of the seasonal $|\Pi|$

cycle (Fig. 4, right panels) only approaches 8×10^{-12} m^{-1} s^{-1} and is less for the majority

of grid points. With only $|\Pi|$ values below 50×10^{-12} m^{-1} s^{-1} analyzed, a conservative

estimate of the annual $|\Pi|$ cycle on each grid point is on the order of 10% of the mean,

the ratio being somewhat higher close to the subduction region where lower mean $|\Pi|$

values are found (Figs. 1b and 4, right panels) and at the boundaries where the cycle

amplitude is large.

We discuss these patterns in more detail below. Note that the late winter

subduction time near the formation regions is not always resolved in this analysis because

of the 3-month smoothing scale used and the fact that we do not map into the mixed

layer.

a. Indian Ocean

We select two isopycnals to discuss Indian Ocean SAMW: $\sigma_\theta = 26.68$ kg m^{-3} and 26.78

kg m^{-3} (Fig. 4a - d). These surfaces illustrate the lightest and densest SAMW varieties

that fully lie within the Indian Ocean west of Australia and span a significant area. The

area of low magnitude $|\Pi|$ SAMW with $\sigma_\theta < 26.68$ kg m^{-3} is marginal (Fig. 1a, colors).

We do not discuss further the significant amount of SAMW with $\sigma_\theta > 26.78$ kg m^{-3} that is

formed and stays mainly south of Australia (Fig. 1c, black contours) or is found very

close to the Leeuwin Current just offshore of the west coast of Australia, where it is only

suboptimally resolved by this climatology because of the long zonal scales used in its

construction.

The spatial pattern of the location of the early September $|\Pi|$ minima for the

lighter Indian Ocean SAMW on $\sigma_\theta = 26.68$ kg m^{-3} (Fig. 4a, black patches) clearly

reveals broad bands of phase propagating northwestward. This phase propagation is also

present for the denser Indian Ocean SAMW on $\sigma_\theta = 26.78$ kg m^{-3} (Fig. 4c, black patches),

but is not very clear near the SAMW origin in the southeastern Indian Ocean, perhaps

because the annual cycle varies in location and strength from year-to-year most strongly

near the formation region, disrupting the climatological cycle (here and in the Pacific).

Still, most grid points on this denser surface do have a pronounced annual $|\Pi|$ cycle (Fig.

4b vs. d). In addition, on $\sigma_\theta = 26.78$ kg m^{-3} low $|\Pi|$ SAMW spreads nearly over the

entire subtropical gyre and has mostly substantially lower $|\Pi|$ magnitudes than on $\sigma_\theta =$

26.68 kg m^{-3} (Figs. 1a, b, 4a, c). This denser isopycnal deepens significantly east and

northward around the southwestern tip of Australia, which might be a reason for an

absence of phase propagation pattern south of 32°S. Again, phase propagation is clearer

from 32°S northward on this denser isopycnal.

The rate of phase propagation is nicely revealed by plotting the month of the $|\Pi|$

minimum versus distance (Fig. 5a, b) along paths roughly following geostrophic currents

(Fig. 4a, c, red lines with 1000-km distance stamps). Since we have not constrained our

geostrophic velocities or 1000-dbar reference fields to be non-divergent, streamlines are

difficult to define exactly. However, the paths chosen here, and those used below in the

Pacific, are similar to those estimated from Montgomery streamfunction (or for that

matter Bernoulli potential) in another study of the SAMW (Herraiz-Borreguero and

Rintoul 2011). The analysis suggests a $|\Pi|$ anomaly propagation of ~3000 km in 12

months (~10 cm s^{-1}) north of 35°S for SAMW on $\sigma_\theta = 26.78$ kg m^{-3} and a propagation of

~2000 km in 12 months (~6 cm s^{-1}) south of 30°S for SAMW on $\sigma_\theta = 26.68$ kg m^{-3}. In

general, $|\Pi|$ anomalies appear to propagate within SAMW along Indian Ocean surfaces

($\sigma_\theta = 26.68$ kg m^{-3} and 26.78 kg m^{-3}) with a phase speed of > 5 cm s^{-1} south of 30°S and

~10 cm s^{-1} northward of that latitude (Fig. 5a, b) as suggested by the clearly visible

northwestward spreading $|\Pi|$ bands (Fig. 4a, c).

b. Pacific Ocean

We choose three isopycnals that span the Pacific Ocean SAMW from west to east (Fig.

4e–k): $\sigma_\theta = 26.88$ kg m^{-3}, 26.94 kg m^{-3}, and 26.98 kg m^{-3}. The lightest surface, $\sigma_\theta =$

26.88 kg m^{-3}, falls within the region of thickest vertical levels of SAMW (Fig. 1a) despite

the absence of a pronounced low $|\Pi|$ core there (Fig. 1c). The denser surfaces, $\sigma_\theta = 26.94$

kg m^{-3} and 26.98 kg m^{-3}, are close to or at the two $|\Pi|$ minimums in the central and

eastern South Pacific (Fig. 1b) respectively, and low $|\Pi|$ SAMW on these surfaces

reaches all the way to the west Pacific. Furthermore, low $|\Pi|$ SAMW on $\sigma_\theta = 26.98$ kg

m^{-3} covers the largest area of SAMW on all isopycnal levels considered.

The locations of the September minimum in $|\Pi|$ anomaly on these isopycnals in

the Pacific Ocean (Fig. 4e, g, i) reveal banded patterns similar to those found in the

Indian Ocean.   Again, these patterns of $|\Pi|$ anomaly bands on all isopycnals suggest

north and northwestward phase propagation.

The months of $|\Pi|$ minimum versus distance along two approximate geostrophic

flow pathways on isopycnals (Fig. 5c, d) in the central ($\sigma_\theta = 26.94$ kg m^{-3}) and eastern (σ_θ

= 26.98 kg m^{-3}) South Pacific suggest $|\Pi|$ anomaly propagation of 750 km in 9 months (~

2 cm s^{-1}) south of 40°S for SAMW in the central South Pacific (on σ_θ = 26.94 kg m^{-3})

and similar propagation of 600 km in 9 months (~2 cm s^{-1}) around 50°S in the eastern

South Pacific (on σ_θ = 26.98 kg m^{-3}). North of these latitudes the phase propagation of

$|\Pi|$ anomalies is difficult to discern, but may be considerably faster.

Animations (not shown) of $|\Pi|$ anomaly seasonal cycles on σ_θ = 26.94 kg m^{-3}

26.98 kg m^{-3} suggest a cyclonic-phase propagation roughly following the outer isovorts

of the SAMW considered here. While this pattern is not obvious in the analysis

presented here (Fig. 5c, d) or in the maps of the September minimum $|\Pi|$ anomaly

locations on isopycnals (Fig. 4g, i), it is discussed further below.

5.   Geostrophic spreading

Since SAMW is arguably the most prominent upper-ocean water mass in the Southern

Hemisphere we are interested in its residence times and propagation patterns. Knowing

more about the flow patterns within SAMW can help understanding its role in ventilating

waters below the thermocline, both isopycnally and via diapycnal mixing. We use

geostrophic current estimates to compare observed $|\Pi|$ anomaly propagation with a

dynamically derived flow field (Fig. 4, left panels, green arrows).

The flow fields we use in our analysis are calculated using monthly geostrophic

velocities estimated at 2-dbar pressure intervals and interpolated onto isopycnals. These

flow fields are made absolute using estimates of the velocity at 1000 dbar derived from

float displacement data as explained above.

a. Indian Ocean

Geostrophic currents are similar for both Indian Ocean isopycnals considered here (Fig. 4, left panels, green arrows): northwest turning westward and with increasing velocities from south to north. The northern edge of the eastward-flowing AAC is obvious only south of 45°S on $\sigma_\theta = 26.78$ kg m^{-3} (Fig. 4c), with a rapid transition into northwestward flow immediately north of the ACC. Geostrophic currents are generally orthogonal to bands of $|\Pi|$ anomalies with similar minimum months. Since geostrophic currents and Bernoulli potential will be roughly parallel, this orthogonality would be expected dynamically in the ocean interior from the impermeability theorem (e.g. Maze and Marshall, 2011),

b. Pacific Ocean

All Pacific isopycnals share a geostrophic current feature close to the Eltanin Fracture Zone (about 130°W, 54°S – Smith and Sandwell, 1997) of the East Pacific Rise, which extends as shallow as 750 m in this region. Here the ACC diverts temporarily northward within the SAMW (Fig. 4e, g, i), with apparently wide-reaching effects on the geostrophic flow and perhaps the SAMW distribution. Around 130°W one branch of the geostrophic flow field turns northward over a fairly wide longitude range while another branch continues in a more northeasterly direction on the other side of the East Pacific Rise. The influence of the rise is also apparent in the SAMW thickness minimum (Fig. 1a) and east-west sloping isopycnals, as well as the different core densities of SAMW on either side of the rise (Fig. 1c). On $\sigma_\theta = 26.88$ kg m^{-3} areas with $|\Pi|$ below the low SAMW threshold used here are only found west of this location (Fig. 4e), while $\sigma_\theta = 26.94$ kg m^{-3} (Fig. 4g) and $\sigma_\theta = 26.98$ kg m^{-3} SAMW (Fig. 4i) low $|\Pi|$ areas span both the

Southeast Pacific and Southwest Pacific basins. While the isopycnal in the western South Pacific SAMW (Fig. 4e, $\sigma_\theta = 26.88$ kg m^{-3}) shows mainly the northwest branch of this South Pacific flow field, the other denser isopycnals (Fig. 4g, i) show northwest currents in the west and northeast currents in the east between 50°S and 35°S. The current directions fan around the Eltanin Fracture Zone. The mid-latitude geostrophic currents have higher northward velocities in the east than in the west. North of 35°S currents on all isopycnals accelerate into a westward flow band—the northern limb of the subtropical gyre (Fig. 4e, g, i).

6.   Discussion and Conclusions

Our analysis concentrates on several varieties of SAMW found in the Indian and Pacific oceans, examining properties and flow fields on isopycnals spanning the low $|\Pi|$ cores of these varieties. We focus on the obvious northward and northwestward-moving annual cycle in $|\Pi|$ anomalies on all isopycnals analyzed (Fig. 4, left panels). These patterns suggest, as might be expected, that seasonal $|\Pi|$ propagation after subduction is to a large degree similar each year. Erratic short time-scale or interannually varying SAMW pathways and core properties would work to obscure the $|\Pi|$ phase pattern so apparent in the monthly climatology presented here, thus seasonal processes appear to dominate.

The most obvious $|\Pi|$ anomaly phase propagation pattern for an entire isopycnal within the low $|\Pi|$ SAMW core stands out in the western Indian Ocean SAMW on $\sigma_\theta = 26.68$ kg m^{-3} (Fig. 4a). All other surfaces also include areas with less obvious phase propagation patterns (Fig. 4, other left panels). However, analysis of the months of $|\Pi|$

minimum along approximate flow paths (Fig. 5) does suggest propagation of anomalies in some regions on these isopycnals. The reasons for the less obvious propagation patterns in regions on some isopycnals analyzed here are uncertain, but several factors may contribute.

One likely explanation is that in regions where geostrophic currents are very slow, the horizontal wavelength for seasonal $|\Pi|$ anomalies may approach or fall below the threshold that can be resolved by the mapping scales used to construct the climatology. Alternately, a slower and less well-aligned flow field, as found in the interior of most surfaces studied, could also create convergence or divergence in $|\Pi|$ anomaly phase propagations and thus obscure any obvious patterns. Finally, $|\Pi|$ phase propagation on underlying or overlying SAMW surfaces might cause isopycnal displacements that interfere with $|\Pi|$ phase on the surfaces analyzed (e.g. Fig. 5d).

We do not find a simple correlation between $|\Pi|$ and annual $|\Pi|$ cycle amplitude (not shown). We leave investigation of the apparent amplitude changes in the seasonal $|\Pi|$ anomalies along their propagation paths to the future.

All analyzed SAMW density surfaces show some propagation of $|\Pi|$ phase. To verify whether the $|\Pi|$ propagation corresponds to water mass displacements, we calculate geostrophic currents and superimpose them. For the geostrophic flow and $|\Pi|$ phase propagation speeds to be similar on the isopycnals analyzed, the 2-year current displacement vectors shown (Fig. 4, left panels, green arrows) would need to span two complete wavelengths of $|\Pi|$ seasonal cycles. This criterion is not met on any of the isopycnals. The discrepancy is such that $|\Pi|$ anomaly phase speeds significantly exceed the speeds of geostrophic currents.

Geostrophic currents show northward speeds of < 1 cm s^{-1} close to the formation region, north of the ACC (Fig. 4g, i), increasing up to ~3 cm s^{-1} in the subtropical Pacific Ocean and up to ~5 cm s^{-1} in the subtropical Indian Ocean (Fig. 4, left panels). In general, these geostrophic flows appears to be orthogonal to bands of constant $|\Pi|$ anomaly phase, so the phase propagation is aligned with the geostrophic flow. However, the phase propagation speeds for $|\Pi|$ anomalies are ≤ 2.5 cm s^{-1} close the ACC in the Pacific Ocean increasing northward (Fig. 5c, d) and ~10 cm s^{-1} in the Indian Ocean (Fig. 5a, b). The phase speeds for $|\Pi|$ anomaly propagation, while uncertain, do appear to exceed the geostrophic flow on all isopycnals. Subtracting the geostrophic displacements from these observed phase speeds should yield the approximate wave propagation speeds for a resting ocean. These differences are on the order of 1 cm s^{-1} around 50°–40°S increasing to the order of 2–5 cm s^{-1} in subtropical regions. These wave velocities are close to the westward-propagating baroclinic 2nd mode speeds for a resting ocean as calculated by Thompson and Ladd (2004) who were modeling pycnocline disturbances in the North Pacific Ocean. Downstream of subduction regions, variations in SAMW $|\Pi|$ occur at intermediate depths near the base of the permanent pycnocline, and thus may be best described by a 2nd vertical mode.

Since the annual formation of SAMW along the northern rim of the ACC can be seen as disturbance and water mass displacement by geostrophy can only explain a fraction of the seasonal $|\Pi|$ anomaly movement, it seems likely that the observed phase propagations are indeed the 2nd vertical mode waves, observed here in Argo data.

We mostly neglect the lowest $|\Pi|$ SAMW south of Australia (Fig. 1b, c) and the portion of the eastern South Pacific SAMW that is exported to the South Atlantic via the

Drake Passage. This first neglect is partly justified by the fact that SAMW south of

Australia is of similar or lesser thickness than in the Indian and Pacific oceans (Fig. 1a, c)

and at the same time has a very limited northward reach. Thus SAMW found south of

Australia fills a significantly smaller volume than the other analyzed varieties. The very

low $|\Pi|$ values of SAMW found south of Australia may be explained by annual renewal

without significant northward propagation. This climatology would be pushed beyond its

limit by a thorough analysis of this variety close to the several narrow topographic and

current features, including the ACC, mainland Australia, Tasmania, and New Zealand.

Secondly, the same limitations would apply to the case of the far eastern Pacific SAMW

exported to the Atlantic in terms of Tierra del Fuego, the Falklands, and the ACC, which

is in any event quite distinct (Fig. 1c) from the varieties analyzed here.

References

Cleveland, W. S., and S. J. Devlin, 1988: Locally-weighted regression: An approach to regression analysis by local fitting. *J. Am. Stat. Assoc.*, **83**, 596–610.

Davis, R. E., 2005: Intermediate-depth circulation of the Indian and South Pacific oceans measured by autonomous floats. *J. Phys. Oceanogr.*, **35**, 683–707.

Hanawa, K., and L. D. Talley, 2001: Mode Waters. In *Ocean Circulation and Climate: Observing and Modelling the Global Ocean*, Siedler, G., J. Church, and J. Gould eds., Academic Press, San Diego, 373–386.

Herraiz-Borreguero, L., and S. R. Rintoul, 2011: Subantarctic mode water: distribution and circulation, *Ocean Dynam.*, **61**, 103–ß126

Karstensen J., and D. Quadfasel, 2002: Formation of Southern Hemisphere thermocline waters: Water mass conversion and subduction. *J. Phys. Oceanogr*., **32**, 3020–3038.

Koch-Larrouy A., R. Morrow, T. Penduff, and M. Juza, 2010: Origin and mechanism of Subantarctic Mode Water formation and transformation in the southern Indian Ocean. *Ocean Dynam.*, **60**, 563–583.

Lebedev K., H. Yoshinari, N. A. Maximenko, and P. W. Hacker, 2007: *YoMaHa'07: Velocity data assessed from trajectories of Argo floats at parking level and at the sea surface*. IPRC Technical Note No. 4(2), 16 pp.

Lozier, M. S., M. S. McCartney, and W. B. Owens, 1994: Anomalous anomalies in averaged hydrographic data. *J. Phys. Oceanogr*, **24**, 2624–2638.

Maze, G., and J. Marshall, 2011: Diagnosing the observed seasonal cycle of Atlantic subtropical mode water using potential vorticity and its attendant theorems. *J. Phys. Oceanogr.*, in press, doi: 10.1175/2011JPO4576.1

McCartney M. S., 1977: Subantarctic Mode Water. In "*A Voyage of Discovery: George Deacon 70th Anniversary Volume (supplement to Deep–Sea Res.)*", M. V. Angel, ed., Pergamon Press, Oxford, 103–119.

Pedlosky, J., 1987: *Geophysical Fluid Dynamics*. Springer–Verlag, New York, 2nd ed., 710 pp.

Rintoul, S. R., and M. H. England, 2001: Ekman transport dominates local air-sea fluxes in driving variability of Subantarctic Mode Water. *J. Phys. Oceanogr.*, **32**, 1308–1321.

Roemmich, D., G. C. Johnson, S. Riser, R. Davis, J. Gilson, W. B. Owens, S. L. Garzoli, C. Schmid, and M. Ignaszewski, 2009: The Argo Program: Observing the global ocean with profiling floats. *Oceanography*, **22** (2), 34–43.

Sallee, J. B., N. Wienders, K. Speer, and R. Morrow, 2006: Formation of subantarctic mode water in the southeast Indian Ocean. *Ocean Dynam.*, **56**, 525–542.

Sallee, J. B., K. Speer, R. Rintoul, and S. Wijfels, 2010: Southern Ocean thermocline ventilation. *J. Phys. Oceanogr.*, **40**, 509–529.

Seitz, R. C., 1967: Thermostad, the antonym of thermocline. *J. Mar. Res.*, **25**, 203.

Sloyan, B. M., L. D. Talley, T. K. Chereskin, R. Fine, and J. Holte, 2010: Antarctic Intermediate Water and Subantarctic Mode Water formation in the southeast Pacific: The role of turbulent mixing. *J. Phys. Oceanogr.*, **40**, 1558–1574.

Smith, W. H. F., and D. T. Sandwell, 1997: Global seafloor topography from satellite altimetry and ship depth soundings. *Science*, **277**, 1957–1962.

Stommel, H., 1979: Determination of water mass properties of water pumped down from the Ekman layer to the geostrophic flow below. *Proc. Natl. Acad. Sci.*, **76**, 3051–3055.

Thompson L., and C. A. Ladd, 2004: The response of the North Pacific Ocean to decadal variability in atmospheric forcing: Wind versus buoyancy forcing. *J. Phys. Oceanogr.*, **34**, 1373–1386.
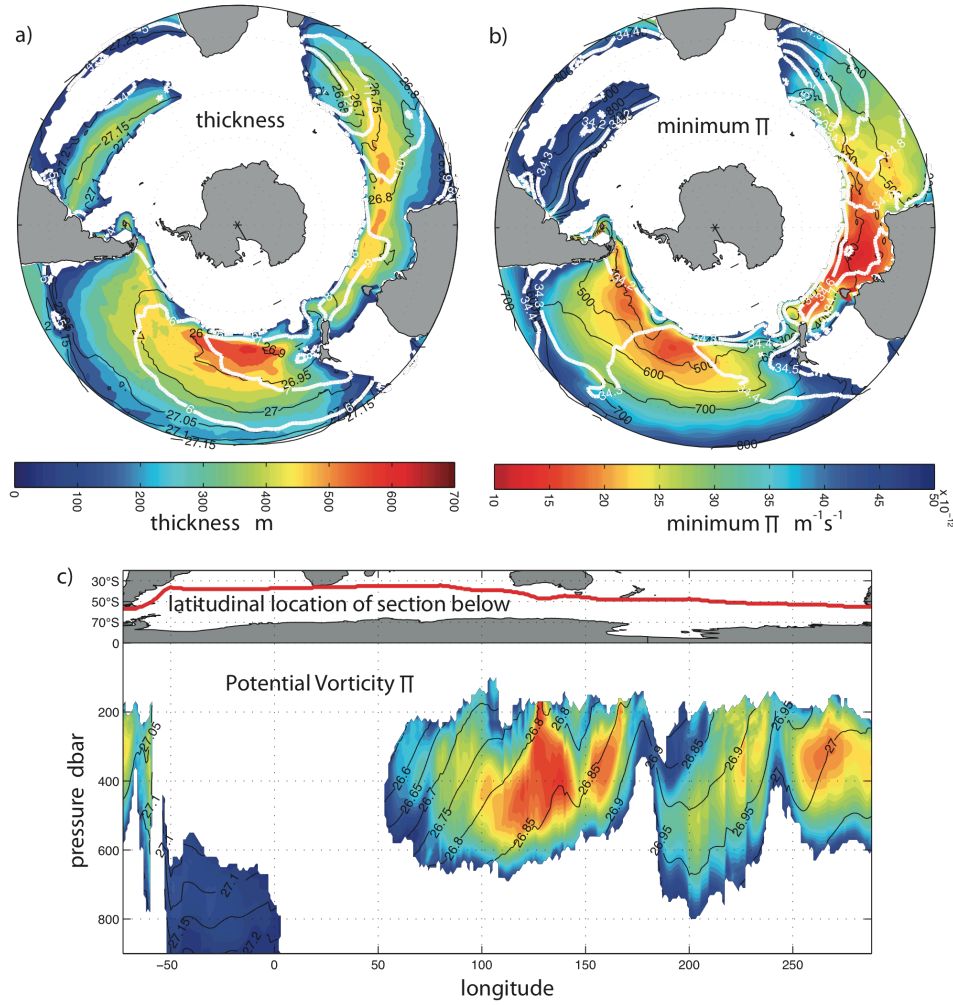
FIG. 1. (a) Annual mean thickness of Subantarctic Mode Water (SAMW) in colors. Core isopycnals and isotherms are superimposed in black and white contour lines, respectively. (b) Annual mean potential vorticity ($|\Pi|$) of SAMW in colors. Core isobars and isohalines are superimposed in black and white contour lines, respectively. (c) Section of annual mean $|\Pi|$ of SAMW along the smoothed meridional $|\Pi|$ minimum latitude in colors following (b). Location of that latitude indicated by red line on superimposed map near the top of the panel. Black contour lines show isopycnals. Data only displayed for areas with $|\Pi| < 50 \times 10^{-12}$ m^{-1} s^{-1} for more than four months out of 12.
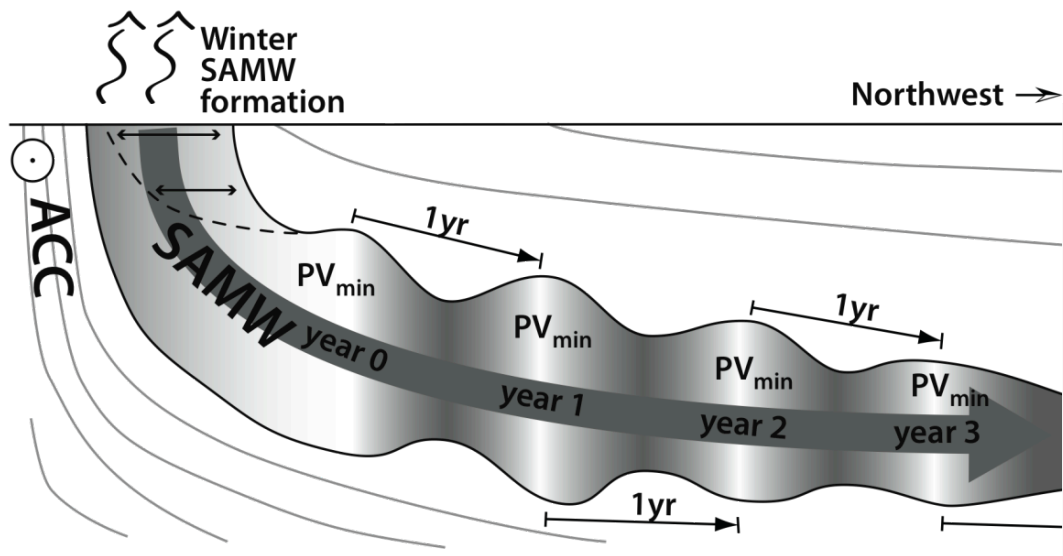
FIG. 2. Schematic of propagation of annually formed SAMW $|\Pi|$ minima anomalies propagating northwesterly from their source region at the base of the subtropical thermocline – proverbial $|\Pi|$ anomaly pigs in the SAMW python. Winter formation region is below curved arrows signifying air-sea exchanges with straight lateral arrows adjacent to the dashed line schematizing near-surface meridional seasonal isopycncal excursions.
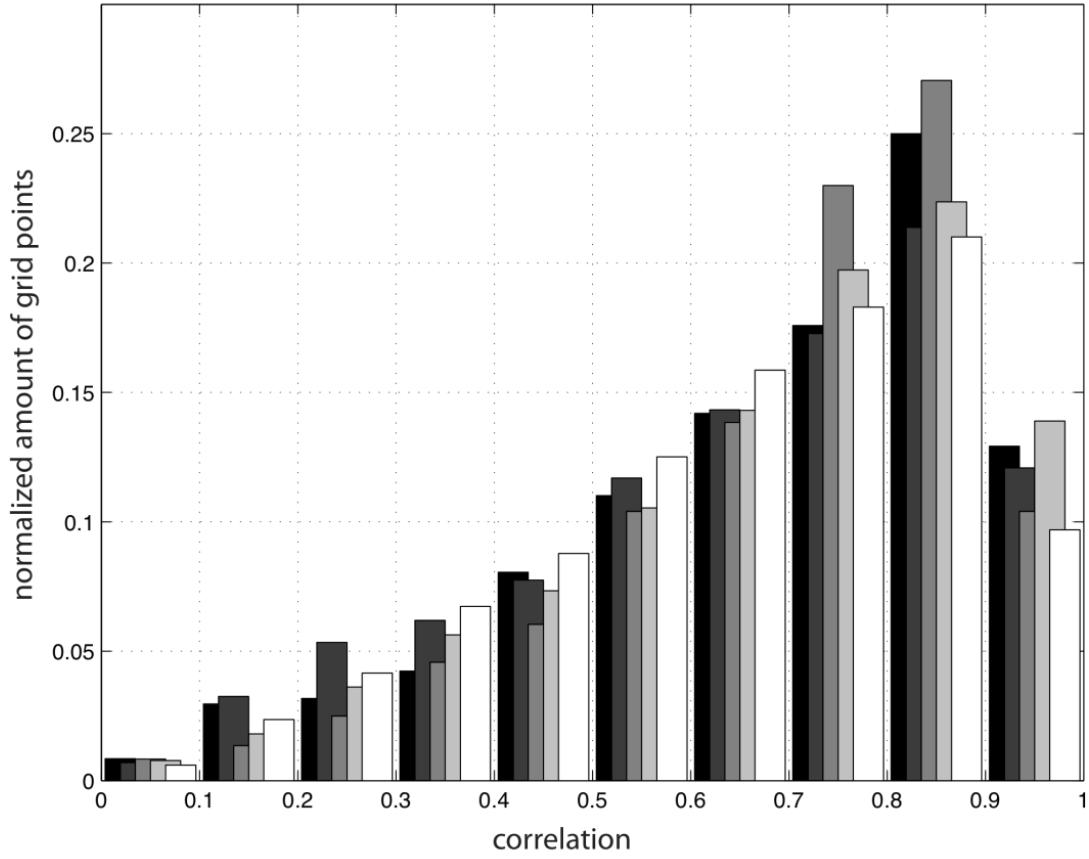
FIG. 3. Histogram of maximum correlation with the annual harmonic for each analyzed

isopycnal within the SAMW definition threshold, normalized by the total number of

climatological grid points within the SAMW for that isopycnal. Ordered from lightest

Indian Ocean isopycnal in white ($\sigma_\theta = 26.68$ kg m^{-3}) successively to densest Pacific

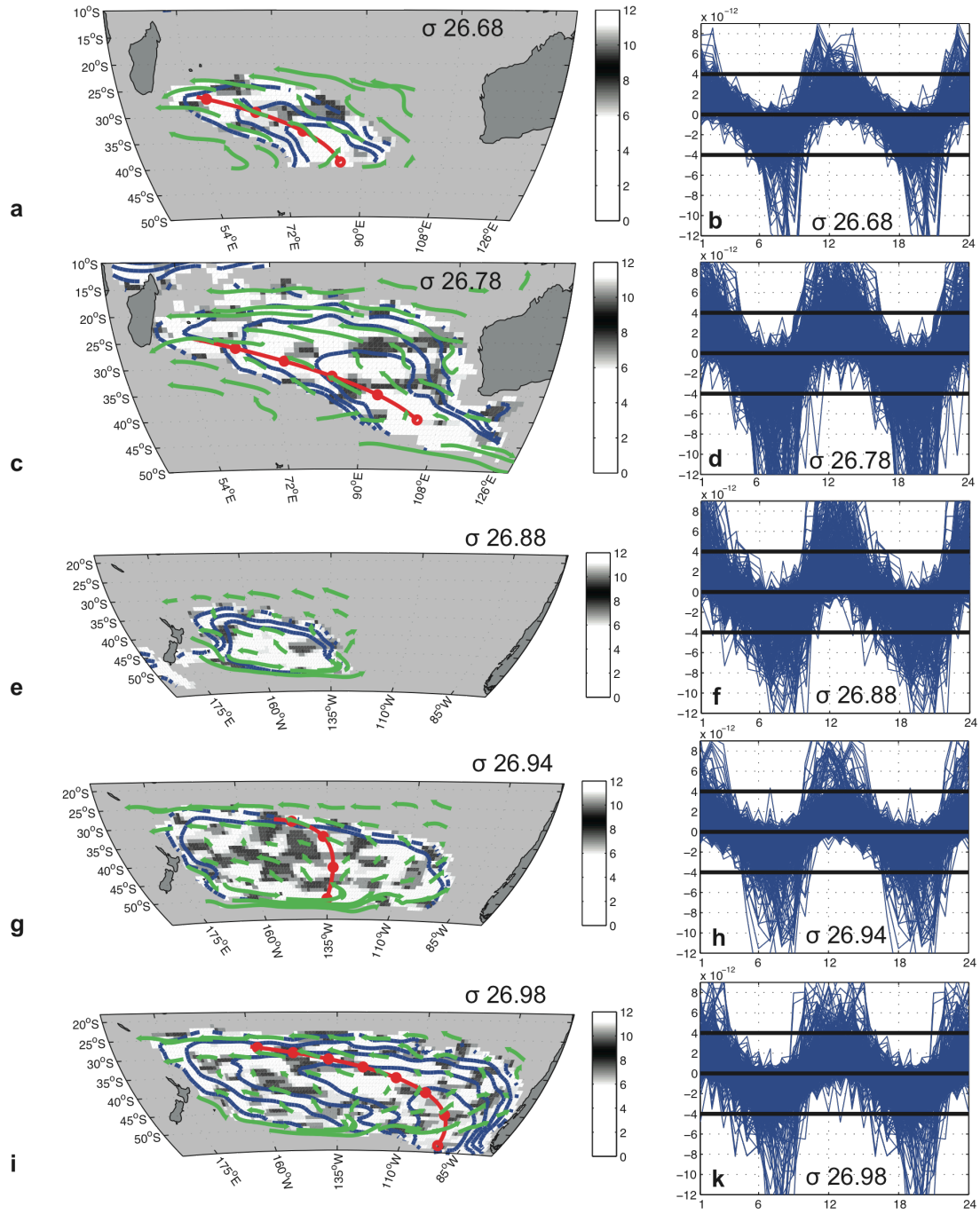isopycnal in black ($\sigma_\theta = 26.98$ kg m^{-3}).

FIG. 4. Locations of the early September $|\Pi|$ minimum (gray shading) from an annual harmonic fit to monthly climatology data on five selected isopycnals in the Indian and Pacific oceans in the left panels (a, c, e, g, i). Two-year geostrophic displacements are overlaid as green arrows as are $|\Pi|$ isovorts at 5×10^{-12} m^{-1} s^{-1} intervals in blue contours,

with 45×10^{-12} m^{-1} s^{-1} being the largest, outermost isovort. An arrow with a length of 5°

latitude represents a mean geostrophic current of ~1 cm s^{-1}. Approximate flow paths

examined in detail in Fig. 5 are given by red lines, with circles marking every 1,000 km.

Areas without year-round presence of SAMW are masked. Right panels (b, d, f, h, k)

repeat the potential vorticity anomalies over the two climatological years for each 1° × 1°

grid point in the corresponding left panel with correlation above 0.4. Each cycle is

temporally shifted to its maximum correlation with an annual harmonic so that local

phases match up for this global representation. Black lines at -4, 0 and 4 ($\times 10^{-12}$ m^{-1} s^{-1})
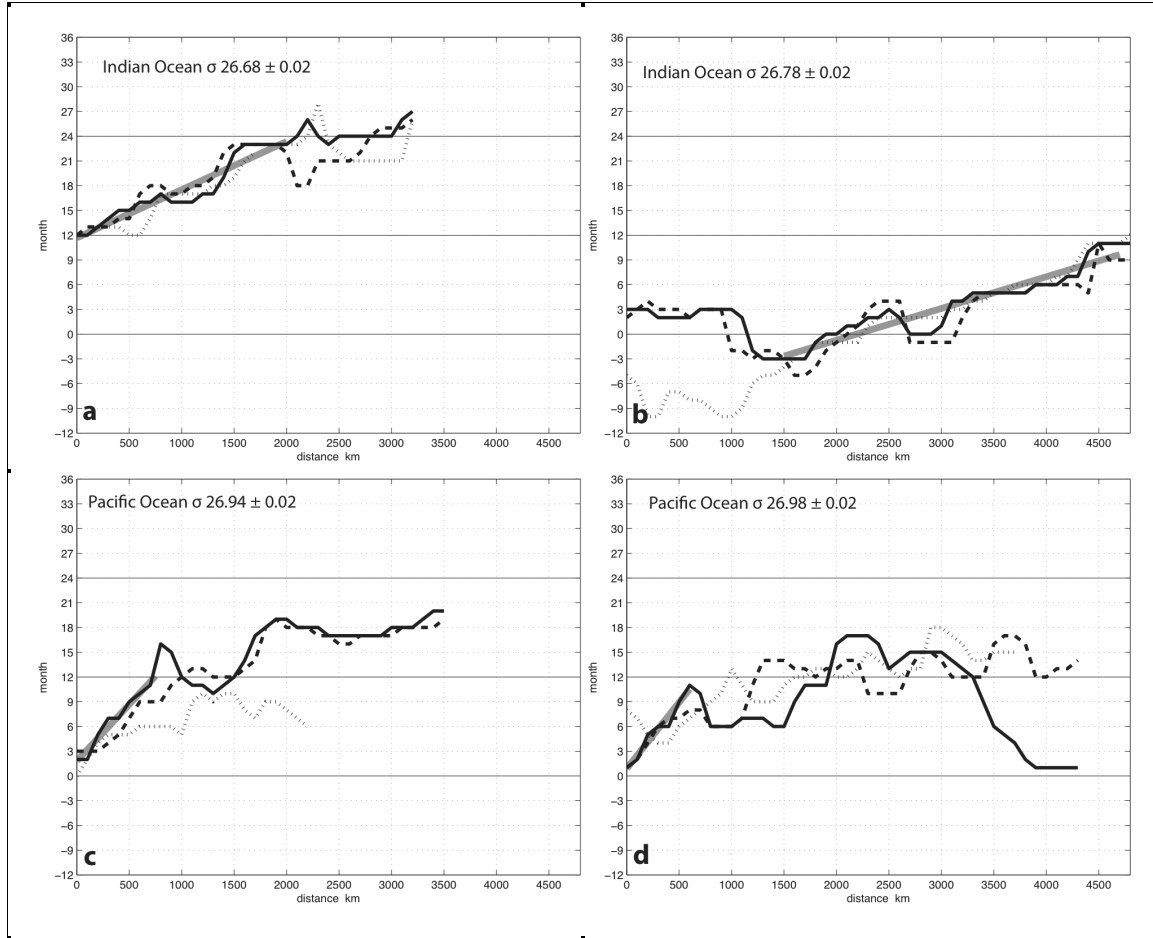
are for reference purposes.

FIG. 5. Month of the minimum $|\Pi|$ anomaly from a fitted annual harmonic along approximate flow pathways on four isopycnals (indicated by red lines in Fig. 4a, c, g, and i, respectively). The time values have been unwrapped, e.g. made continuous with 12-month offsets as needed. Black lines reference the isopycnals analyzed, while the dotted and dashed lines reference the over and underlying isopycnal layers for the climatology. Thick grey lines fit to values for portions of the pathways illustrate propagation speeds.